Ideal conductor/dielectric model (ICDM): A generalized technique to correct for finite-size effects in molecular simulations of hindered ion transport

Brian A Shoemaker[1] and Amir Haji-Akbari[1,*]

[1]*Department of Chemical and Environmental Engineering, Yale University, New Haven, CT 06520*

(Dated: October 6, 2023)

Molecular simulations serve as indispensable tools for investigating the kinetics and elucidating the mechanism of hindered ion transport across nanoporous membranes. In particular, recent advancements in advanced sampling techniques have made it possible to access translocation timescales spanning several orders of magnitude. In our prior study (Shoemaker, *et al.*, *J. Chem. Theory Comput.*, 18: 7142, **2022**), we identified significant finite size artifacts in simulations of pressure-driven hindered ion transport through nanoporous graphitic membranes. We introduced the ideal conductor model, which effectively corrects for such artifacts by assuming the feed to be an ideal conductor. In the present work, we introduce the ideal conductor dielectric model (ICDM), a generalization of our earlier model, which accounts for the dielectric properties of both the membrane and the filtrate. Using the ICDM model substantially enhances the agreement among corrected free energy profiles obtained from systems of varying sizes, with notable improvements observed in regions proximate to the pore exit. Moreover, the model has the capability to consider secondary ion passage events, including the transport of a co-ion subsequent to the traversal of a counter-ion, a feature absent in our original model. We also investigate the sensitivity of the new model to various implementation details. The ICDM model offers a universally applicable framework for addressing finite size artifacts in molecular simulations of ion transport. It stands as a significant advancement in our quest to use molecular simulations to comprehensively understand and manipulate ion transport processes through nanoporous membranes.

I. INTRODUCTION

Hindered ion transport through nanopores is a ubiquitous phenomenon and occurs in a wide variety of systems, including channel proteins in biological membranes,[1,2] ion separation membranes in batteries[3,4] and fuel cells,[5] and polymeric membranes in reverse osmosis water desalination.[6] In all these cases, the ability of constituent nanopores to modulate ion transport is key to their respective function, and understanding the relationship between nanopore structure and ion transport kinetics and mechanism is key to engineering such systems. Unfortunately, it is extremely challenging to characterize structure-selectivity relationship using experiments due to the limited spatiotemporal resolution of the existing experimental techniques. As such, molecular simulations have emerged as attractive tools for conducting systematic studies in which the effect of hypothesis-driven perturbations to nanopore chemistry and geometry is investigated on the transport of different ions.[7]

The prime example of this is water desalination. Water sustainability is one of the grand challenges of our era, as almost 40% of the world's population lack adequate access to sources of clean freshwater,[8] and this is only going to exacerbate considering current trends in population growth,[9] urbanization,[10] and climate change.[11] In recent decades, water desalination has emerged as a core technology in this quest, and it produces 95 million m^3/day of purified water.[12] In particular, reverse osmosis, which is based on using nanoporous water-permeable membranes to reject ions and small molecules, constitutes a particularly efficient means of carrying out desalination.[13] Despite its promise, there are still significant technological barriers to widespread adoption of reverse osmosis desalination such as high energy requirements,[13] environmental concerns with the disposal of high-concentration brine,[14] and capital costs due to membrane fouling and degradation.[15] Improving the efficacy of reverse osmosis desalination therefore requires developing novel membranes with enhanced properties, most notably high permeability to water and strong rejection of small ions and molecules. In an effort to solve this complicated optimization problem, molecular simulations have proven indispensable, providing valuable insights about nanoporous membranes based on graphene,[16–20] metal-organic frameworks (MOFs),[21] and polymers.[22,23]

A second example is biological channel proteins, which modulate the transport of ions through cellular and organellar membranes. They generally possess extraordinary levels of ion-water and ion-ion selectivity, yet there are significant gaps in our understanding of the molecular origins of such selectivity. Similar to water desalination, various techniques in molecular simulations have been used to investigate different aspects of water and ion transport through channel proteins,[24] such as aquaporins[25–27] and the potassium channel.[28,29]

Despite their potential, the accuracy of molecular simulations depends on a multitude of implementation details. One such detail is the need to conduct molecular simulations within nanoscale simulation boxes and to employ periodic boundary conditions to avoid interfacial artifacts. In particular, typical systems considered

*Corresponding Author:amir.hajiakbaribalou@yale.edu

in atomistic simulations are comprised of $\sim 10^4 - 10^5$ atoms. They therefore always exhibit deviations from what would be expected in the thermodynamic limit (assuming the validity of the employed force-field and the fidelity of other implementation details). Such deviations are referred to as *finite size effects* and have been documented for a variety of properties, such as diffusivity,[30,31] radial distribution function and structure factor,[32] relaxation times in glassy systems,[33] thermal conductivity,[34] piezoelectric response,[35] and crystal nucleation rates.[36,37] Finite size effects can be particularly atrocious for rare events, i.e., collective phenomena that involve crossing large free energy barriers.

A notable– and unfortunate– example is hindered ion transport through membranes. In our earlier work,[19] we demonstrated that the kinetics and mechanism of pressure-driven chloride transport through nanoporous graphitic membranes is strongly impacted by the size of the simulation box. In particular, we observed ionic fluxes to change by almost six orders of magnitude within the range of system sizes considered therein. By assuming that the electrolytic feed compartment is an ideal conductor, we analytically derived and numerically validated a model to correct for finite size artifacts. This work seeks to improve and generalize the model of Ref. 19 by incorporating additional physics pertaining to induced charges in dielectric regions such as the membrane and the filtrate. The new model, which we call the *ideal conductor/dielectric model (ICDM)*, systematically considers the impact of dielectric-dielectric interfaces on the free energy correction. One of the important practical advantages of the ICDM model is its ability to properly handle secondary ion transport processes wherein one or more ions have previously traversed the membrane prior to the translocation of the ion of interest.

This paper is organized as follows. The theoretical framework for constructing the ICDM correction is laid out in Section II, with Sections II A and II B devoted to the method of images and the construction of the free energy correction, respectively. Details of system setup, molecular dynamics simulations and rate calculations are outlined in Section III. Section IV details our numerical validation of the ICDM model, particularly its extension to secondary ion translocation events. We present our concluding remarks in Section V.

II. THE IDEAL CONDUCTOR/DIELECTRIC MODEL (ICDM)

The original *ideal conductor model* (presented in Ref. 19) treats the feed compartment as an ideal conductor and the membrane region as a region with dielectric constant $\epsilon_r = 1$. Therefore, when an ion leaves the feed (e.g., as a result of a hydrostatic or osmotic pressure gradient), it induces a charge surplus (or deficit) within the conductor, which then accumulates at its surface. In the simple case of semi-infinite conducting and dielectric slabs, the surface density of the induced charge can be readily estimated from the method of images. Due to periodic boundary conditions, the periodic replicates of the leading ion will also induce their respective charge densities at the surface of the conductor, which will then exert an unphysical restraining force on the leading ion. The contribution of these periodic replicates to free energy is estimated by computing the change in the electrostatic potential of a fictitious ion moving from pore entrance to the position of the leading ion under the influence of the charge arrangement induced by periodic replicates. The correction to free energy is given by:

$$\begin{aligned}\Delta\mathcal{F}_{\text{corr}}(z) \;=\; & \frac{e^2}{2\epsilon_0 L_x L_y}\Bigg\{ z - z_0 \\ & - \frac{L_x L_y}{2\pi}\left[\frac{1}{z_0 + z} - \frac{1}{2z_0}\right] \\ & - 2\sum_{\alpha\in\{x,y\}}\sum_{k_\alpha=1}^{\infty}\frac{e^{-2q_\alpha z} - e^{-q_\alpha(z+z_0)}}{q_\alpha} \\ & - 4\sum_{k_x,k_y=1}^{\infty}\frac{e^{-2|\mathbf{q}|z} - e^{-|\mathbf{q}|(z+z_0)}}{|\mathbf{q}|}\Bigg\} \end{aligned} \tag{1}$$

Here, ϵ_0 is the vacuum permittivity, and L_x and L_y are the dimensions of the membrane. $\mathbf{q} = 2\pi(k_x/L_x, k_y/L_y)$ is the wavevector associated with $(k_x, k_y) \in \mathbb{Z}^2$. z and z_0 correspond to the position of the leading ion and the point at which the correction starts being applied, respectively. They are both measured with respect to the surface of the conductor. The translocation free energy profile in the thermodynamic limit, $\mathcal{F}_\infty(z)$, is then estimated as

$$\mathcal{F}_\infty(z) \;=\; \mathcal{F}_f(z) - \Delta\mathcal{F}_{\text{corr}}(z) \tag{2}$$

wherein $\mathcal{F}_f(z)$ is the free energy profile obtained from a finite simulation (with box dimensions L_x and L_y). We demonstrate in Ref. 19 that the corrected free energy profiles obtained using (1) exhibit remarkable consistency across different system sizes, leading to translocation barriers that vary by less than one k_BT. The agreement, however, worsens beyond the locus of the translocation barrier, and towards the pore exit. The focus of this work is to rectify these minor (but statistically significant) discrepancies by deriving a generalized model that accounts for dielectric heterogeneities within the system. Doing so requires solving the Poisson's equation within a simulation domain with dielectric heterogeneity, and using that solution to account for the spurious impact of periodic replicates on the translocation free energy profile. Below, we outline both these steps in detail.

A. Solving Poisson's Equation using the Method of Images

In order to account for dielectric heterogeneities, we assume that a typical membrane separation system is comprised of a conducting slab (containing the feed elec-

trolyte) adjacent to a series of dielectric slabs (representing the membrane interior and the filtrate) separated by sharp boundaries. Depending on the progress of translocation, the ion of interest will be in one of these dielectric regions. At an interface separating two domains with dielectric constants $\epsilon_1 \neq \epsilon_2$, the electrostatic potential $\varphi(\mathbf{r})$ will be a continuous function of $\mathbf{r}$. Its first normal derivative, however, will be discontinuous and will satisfy the following boundary condition:

$$\epsilon_2 \left.\frac{\partial \varphi_2}{\partial n}\right|_i - \epsilon_1 \left.\frac{\varphi_1}{\partial n}\right|_i = \sigma_{f,i} \tag{3}$$

Here, $\partial\varphi/\partial n = \mathbf{n}\cdot\nabla\varphi$ is the normal derivative of φ (i.e., along the unit vector $\mathbf{n}$ perpendicular to the interface and pointing towards region 2). The subscript i refers to the fact that both derivatives are evaluated at respective sides of the interface. $\sigma_{f,i}$ is the free charge density at the interface, which is usually zero in membrane separation systems. Note that (3) implies the continuity of the displacement vector ($\mathbf{D} = \epsilon\mathbf{E} = -\epsilon\nabla\varphi$) across interfaces that lack free charges. For an arbitrary arrangement of regions, Poisson's equation can be solved numerically to obtain $\varphi(\mathbf{r})$ throughout the entire simulation domain. In situations wherein the system can be partitioned into dielectric domains separated by parallel flat infinitely-large interfaces, the task of solving the Poisson's equation can be simplified considerably by using the *method of images*. The method seeks to identify a proper collection of surrogate charges outside the region of interest in a manner that yields a solution that satisfies all relevant boundary conditions. The uniqueness property of Poisson's equation will then guarantee that the electrostatic potential of the surrogate system within the appropriate domain is identical to that of the original system.

The simplest case involves an interface that separates two semi-infinite dielectric media with dielectric constants $\epsilon_1 \neq \epsilon_2$ (Figure 1A). If a point charge q is located within the second region and at a distance h from the interface, the method of images can be readily applied as follows. For region 1, $\varphi(\mathbf{r})$ can be determined by considering a system with a charge $q' \neq q$ at the location of the original point charge q (Figure 1B). Similarly, the potential within region 2 can be determined from a system consisting of the original charge q and an image charge q_L which is reflected across the interface (Figure 1C). Such surrogate arrangements will yield the following solution for $\varphi(r)$:

$$\varphi(\mathbf{r}) = \begin{cases} \dfrac{1}{4\pi\epsilon_0\epsilon_1}\dfrac{q'}{|\mathbf{r}-h\mathbf{e}_z|} & z < 0 \\ \dfrac{1}{4\pi\epsilon_0\epsilon_2}\left[\dfrac{q}{|\mathbf{r}-h\mathbf{e}_z|} + \dfrac{q_L}{|\mathbf{r}+h\mathbf{e}_z|}\right] & z \geq 0 \end{cases} \tag{4}$$

By enforcing the continuity of $\varphi(\cdot)$ as well as the boundary condition given by Eq. (3), one can demonstrate that q' and q_L will be given by:

$$q' = \frac{2\epsilon_1 q}{\epsilon_1+\epsilon_2} \tag{5}$$

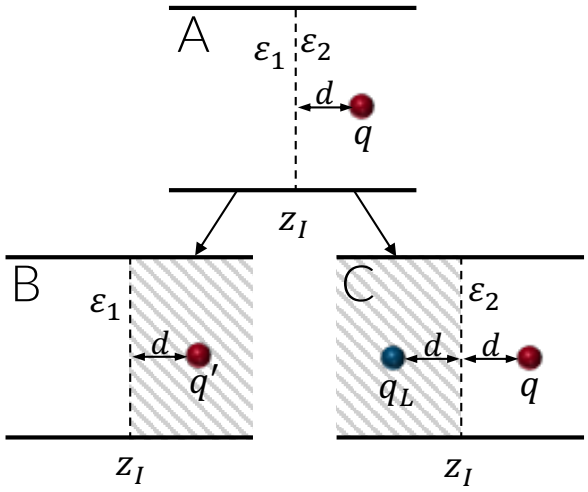

FIG. 1: Schematic representation of the application of the method of images to two adjacent dielectric regions with dielectric constants ϵ_1 and ϵ_2. To accurately represent the actual charge distribution depicted in (A), where a point charge exists in region 2, surrogate charge configurations are devised for regions 1 (B) and 2 (C). In each panel, the solution of the Poisson equation within the white region is determined by the real charge(s) within that region along with the image charge(s) situated within the dashed region.

$$q_L = -\frac{q(\epsilon_1-\epsilon_2)}{\epsilon_1+\epsilon_2} \tag{6}$$

While these simulated image charges effectively reproduce the correct electrostatic potential within both regions, it is crucial to recognize that they do not represent real charges present in the system. Instead, they happen to produce an identical potential to the one generated by the actual charges induced at the dielectric interface. By applying Gauss's law at the interface, using the potential given by Eq. (4), we can deduce that the net charge induced at the interface is given by:

$$q_b = -\frac{q}{\epsilon_2}\left(\frac{\epsilon_1-\epsilon_2}{\epsilon_1+\epsilon_2}\right) \tag{7}$$

It is important to note that the ideal conductor model described in Ref. 19 can be seen as a special case of this approach when $\epsilon_1 \to \infty$ and $\epsilon_2 = 1$. In a broader context, if the first region is considered an ideal conductor, the total induced charge at the surface would be $-q/\epsilon_2$, which is smaller in magnitude than the charge of the leading ion due to electrostatic screening by region 2. However, given that the feed possesses either a surplus or deficit of charge depending on the sign of q, one must distribute the charge $-q\left[1-\epsilon_2^{-1}\right]$ uniformly across the surfaces of the conducting slab.

This two-region model is expected to provide a reasonably accurate representation for scenarios in which the transition state is significantly distant from the pore exit. A more rigorous treatment will, however, require

Algorithm 1 Create image charges for m dielectric regions.

Procedure CreateImageCharges $(\{\epsilon_i\}_{i=1}^{m}, \{z_i\}_{i=1}^{m-1}, q, z_q)$
Inputs:
1. $\{\epsilon_i\}_{i=1}^{m}$, dielectric constants of consecutive regions.
2. $\{z_i\}_{i=1}^{m-1}$, positions of interfaces separating regions i and $i+1$ with $z_1 < z_2 < \cdots < z_{m-1}$.
3. q, magnitude of the point charge.
4. z_q, position of the point charge.

Output: $\{(q_{i,j}, z_{i,j})\}_{j=1}^{n_i}$, the list of magnitudes and positions of all image charges within all regions ($1 \le i \le m$). n_i is the total number of charges associated with region i
Denote the region that q belongs to as i_0.
for $i = 1, 2, \cdots, m$ **do**
  if $i \neq i_0$ **then**
    $\mathcal{L}_i := \{\}$.
  else
    $\mathcal{L}_i := \{(q, z_q, \mathbf{b}_q)\}$. ▷ Assign $\mathbf{b}_q$ using Eq. (14).
  end if
end for
threshold = **true**.
while threshold **do**
  Let $\mathcal{R}_i := \{\}$ for $1 \le i \le m$. ▷ List of reflectable charges in region i.
  for $i = 1, \cdots, m$ **do**
    for $j = 1, \cdots, n_i$ **do**
      if $\mathbf{b}_{i,j}$ has any **true** flag, append $q_{i,j}$ to $\mathcal{R}_i$.
    end for
  end for
  for $i = 1, 2, \cdots, m$ **do**
    for $q' \in \mathcal{R}_i$ **do**
      if $b_{l,q'}$ **then**
        Reflect q' across region i's left boundary, and append the arising charge $\widetilde{q} = -\gamma_{i-1,i} q'$ to $\mathcal{L}_i$.
        Set the reflectivity of $\widetilde{q}$ to $(\mathbf{F}, \mathbf{T})$ and $(\mathbf{F}, \mathbf{F})$ for $i < m$ and $i = m$, respectively.
        Append $\overline{q} = \lambda_{i,i+1} q'$ located at the position of q' to $\mathcal{L}_{i-1}$.
        Set the reflectivity of $\overline{q}$ to $(\mathbf{T}, \mathbf{F})$ and $(\mathbf{F}, \mathbf{F})$ for $i \neq 2$ and $i = 2$, respectively.
        $n_i := n_i + 1$.
        $n_{i-1} := n_{i-1} + 1$.
      end if
      if $b_{r,q'}$ **then**
        Reflect q' across region i's right boundary, and append the arising charge $\widetilde{q} = -\gamma_{i+1,i} q'$ to $\mathcal{L}_i$.
        Set the reflectivity of $\widetilde{q}$ to $(\mathbf{T}, \mathbf{F})$ and $(\mathbf{F}, \mathbf{F})$ for $i > 1$ and $i = 1$, respectively.
        Append $\overline{q} = \lambda_{i+1,i} q'$ located at the position of q' to $\mathcal{L}_{i+1}$
        Set the reflectivity of $\overline{q}$ to $(\mathbf{F}, \mathbf{T})$ and $(\mathbf{F}, \mathbf{F})$ for $i \neq m-1$ and $i = m-1$, respectively.
        $n_i := n_i + 1$.
        $n_{i+1} := n_{i+1} + 1$.
      end if
      $\mathbf{b}_{q'} := (\mathbf{F}, \mathbf{F})$. ▷ This charge can no longer be reflected.
    end for
  end for
  Set threshold := **false** if all boundary conditions (for φ and $\partial\varphi/\partial z$) are satisfied at all interfaces.
end while

considering a minimum of three regions with dielectric constants ϵ_1, ϵ_2 and ϵ_3 for the feed, membrane and filtrate, respectively. (Note that a feed occupied by a sufficiently concentrated electrolytic solution can still be considered an ideal conductor with $\epsilon_1 \to \infty$.) Unfortunately, no simple analytical solution exists for such a tripartite arrangement, and the application of the method of images involves a recursive process in which a series of image charges are introduced in an appropriate manner in order to construct a series solution for the Poisson's equation.

Assuming that a point charge q is located with region 2 (of finite thickness w) and at a distance $h < w$ from the interface with region 1 (Figure 2), one can recursively introduce a sequence of image charges for each region as follows. First, the point charge q is reflected across the boundaries, yielding the image charges $q_{L,1} = -\gamma_{12} q$ and $q_{R,1} = -\gamma_{32} q$ in regions 1 and 3, respectively, with γ_{ij} given by:

$$\gamma_{ij} = \frac{\epsilon_i - \epsilon_j}{\epsilon_i + \epsilon_j} \tag{8}$$

Simultaneously, image charges $q' = \lambda_{12} q$ and $q'' = \lambda_{32} q$ appear in region 2 at the same location as the original charge q with λ_{ij} given by:

$$\lambda_{ij} = \frac{2\epsilon_i}{\epsilon_i + \epsilon_j} \tag{9}$$

Note that both $q_{L,1}$ and $q_{R,1}$ are image charges associated with region 2 while q' and q'' belong to regions 1 and 3, respectively. While each reflection aims to balance its respective interface, it creates imbalance at the other interface. Consequently, an additional round of reflections of $q_{R,1}$ and $q_{L,1}$ is required across the 1/2 and 2/3 interfaces, respectively, resulting in the creation of $q_{L,2} = -q_{R,1}\gamma_{12}$ and $q_{R,2} = -q_{L,1}\gamma_{32}$. Furthermore, extra image charges $q'_{R,1} = \lambda_{12} q_{R,1}$ and $q''_{L,1} = \lambda_{32} q_{L,1}$ are introduced at the same positions as $q_{R,1}$ and $q_{L,1}$. This process can be continued indefinitely to place image charges $q_{L,j}$ and $q_{R,j}$ (alongside their screened counterparts $q''_{L,j}$ and $q'_{R,j}$) at the following positions,

$$z_{L,j} = (-1)^j h + \left[\frac{1-(-1)^j}{2} - j\right] w, \tag{10a}$$

$$z_{R,j} = (-1)^j h + \left[\frac{1-(-1)^j}{2} + j\right] w, \tag{10b}$$

and magnitudes,

$$q_{L,j} = -\gamma_{12} q_{R,j-1}, \tag{11a}$$

$$q_{R,j} = -\gamma_{32} q_{L,j-1}, \tag{11b}$$

$$q'_{R,j} = \lambda_{12} q_{R,j-1}, \tag{11c}$$

$$q''_{L,j} = \lambda_{32} q_{L,j-1}. \tag{11d}$$

Note that $q_{R,0} = q_{L,0} = q$. With these image charges at hand, the solution of Poisson's equation within each region will be given by,

$$\varphi_1(\mathbf{r}) = \frac{1}{4\pi\epsilon_0\epsilon_1} \sum_{j=1}^{\infty} \frac{q'_{R,j}}{|\mathbf{r} - z_{R,j-1}\mathbf{e}_z|} \tag{12a}$$

$$\varphi_2(\mathbf{r}) = \frac{1}{4\pi\epsilon_0\epsilon_2} \left\{ \frac{q}{|\mathbf{r} - h\mathbf{e}_z|} + \sum_{j=1}^{+\infty} \left[\frac{q_{L,j}}{|\mathbf{r} - z_{L,j}\mathbf{e}_z|} + \frac{q_{R,j}}{|\mathbf{r} - z_{R,j}\mathbf{e}_z|} \right] \right\} \tag{12b}$$

$$\varphi_3(\mathbf{r}) = \frac{1}{4\pi\epsilon_0\epsilon_3} \sum_{j=1}^{\infty} \frac{q''_{L,j}}{|\mathbf{r} - z_{L,j-1}\mathbf{e}_z|} \tag{12c}$$

An interesting special case corresponds to when both regions 1 and 3 are ideal conductors. In such a scenario, $\gamma_{12} = \gamma_{32} = 1$, which will imply that all image charges associated with region 2 will be equal in magnitude to q but will have alternating signs. This could potentially impact the convergence of the method adversely. As such, a larger number of image charges might be needed for satisfactory convergence. The electrostatic potential within the dielectric domain will be given by:

$$\varphi_2(\mathbf{r}) = \frac{q}{4\pi\epsilon_0\epsilon_2} \left\{ \frac{1}{|\mathbf{r} - h\mathbf{e}_z|} + \sum_{k=1}^{+\infty} \left[\frac{1}{|\mathbf{r} - (h-2kw)\,\mathbf{e}_z|} + \frac{1}{|\mathbf{r} - (h+2kw)\,\mathbf{e}_z|} - \frac{1}{|\mathbf{r} + [h+2(k-1)w]\,\mathbf{e}_z|} - \frac{1}{|\mathbf{r} + [h-2kw]\,\mathbf{e}_z|} \right] \right\}, \tag{13}$$

which can be readily differentiated to obtain the electric field. Yet, it can be easily demonstrated that the rate of convergence of (13) will be comparable to that of $\sum_{k=1}^{\infty} k^{-2}$ (Appendix A).

In certain scenarios, the inclusion of more than three dielectric regions might become necessary, particularly when the membrane exhibits considerable spatial heterogeneity along the direction of ion transport. While it is not easy to enumerate the sequence of image charges needed for such a scenario, a recursive algorithm (similar to the approach described above) can be formulated to systematically determine the required image charges associated with all regions. Consider a system comprised of m dielectric slabs with dielectric constants $\epsilon_1, \epsilon_2, \cdots, \epsilon_m$, and a point charge q located within region i_0. Our proposed algorithm (Algorithm 1) serves as a robust tool to manage $\mathcal{L}_i$, which contains both real and image charges associated with each region i for $1 \le i \le m$. Each charge within this ensemble is defined not only by its magnitude and position but also by a binary reflectivity vector $\mathbf{b} = (b_l, b_r)$. These reflectivity values, denoted by b_l and b_r, dictate whether a charge will subsequently undergo reflection across the left or right boundary of the region with which it is associated.

At the beginning, $\mathcal{L}_i$'s are all empty except for $\mathcal{L}_{i_0} = \{(q, z_q, \mathbf{b}_q)\}$ wherein $\mathbf{b}_q$ is given by:

$$\mathbf{b}_q = \begin{cases} (\mathbf{F}, \mathbf{T}) & i_0 = 1 \\ (\mathbf{T}, \mathbf{T}) & 1 < i_0 < m \\ (\mathbf{T}, \mathbf{F}) & i_0 = m \end{cases} \tag{14}$$

In each iterative step, a comprehensive scan of all regions is performed to identify charges with at least one **true** reflectivity flag. For every **true** flag, the corresponding charge (associated with region i) is reflected across the respective boundary, generating two image charges. The first charge (with magnitude $-\gamma_{i\pm1,i} q_{\text{orig}}$) is the reflection of the original charge across the respective boundary and is associated with the original region, i. The second charge (with a magnitude $\lambda_{i\pm1,1} q_{\text{orig}}$) is located at the position of the original charge, but is associated with region $i \pm 1$. Once all reflections are completed, all reflectivity flags for the original charges are set to **false**. When it comes to the newly generated image charges, their reflectivity flags are set to **true** except for the boundary across which they were created. It is worth noting that for charges associated with the first and last regions, the first and second flags remain invariably **false**, respectively. For instance, if an image charge associated with

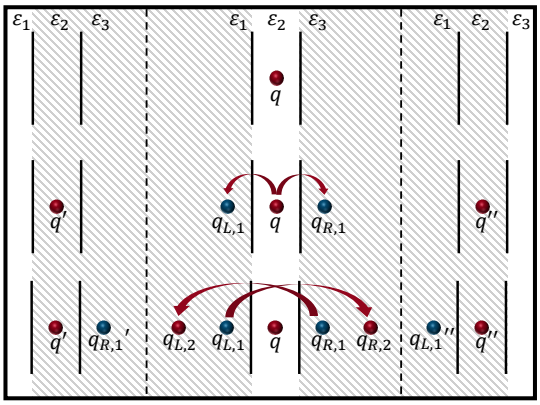

FIG. 2: Illustration of the application of the method of images to a system with three dielectric regions with dielectric constants ϵ_1, ϵ_2, and ϵ_3. A point charge q is located within the central region and is reflected across both boundaries, resulting in the creation of four image charges: two for region 2 and one for each of regions 1 and 3. The two image charges generated within region 2 are further reflected across its second boundary, yielding four additional image charges (two in region 2 and one in each of regions 1 and 3). This recursive process is continued indefinitely, generating a series of image charges as elaborated in the text.

region $1 < i < m$ is reflected across its left boundary, the reflectivity flag of the two new charges (associated with regions i and $i-1$) will be $(\mathbf{F}, \mathbf{T})$ and $(\mathbf{T}, \mathbf{F})$, respectively.

After each iteration, the newly generated image charges are used to update the estimates of the electrostatic potential and its first derivative at every interface. The iterative process concludes when the relative discrepancy between φ and $\epsilon\partial\varphi/\partial n$ (estimated at two sides of every interface) falls below a pre-specified threshold.

B. Constructing the ICDM finite size corrections

The next step is to use the image charges specified in Section II A to derive finite size corrections to free energy. For simplicity, we present the ICDM model within the context of three distinct regions, including an ideal conductor and two dielectric regions. It is, however, important to note that this model can be seamlessly extended to accommodate systems featuring a larger number of dielectric regions, or when both the feed and the filtrate are ideal conductors.

Suppose that an ion with charge q is traversing the membrane and is located at z_l. Let $\{(q_i, z_i)\}_{i=1}^{\infty}$ correspond to the magnitudes and positions of all its image charges. What underlies polarization-induced finite size artifacts is the unphysical excess electric field stemming from all periodic replicates of these images charges, which is given by:

$$E^{\text{ex}}_{\text{pt},z}(z_l) = \sum_{i=1}^{\infty} \sum_{\substack{\mathbf{m}\in\mathbb{Z}^2 \\ \mathbf{m}\neq(\mathbf{0})}} \frac{q_i(z_l - z_i)}{4\pi\epsilon \left[m_x^2 L_x^2 + m_y^2 L_y^2 + (z_l - z_i)^2\right]^{\frac{3}{2}}} \tag{15}$$

Here, $\mathbf{m} = (m_x, m_y) \in \mathbb{Z}^2$ is a pair of integers corresponding to the m_xth and m_yth periodic replicate of each charge along the x and y dimensions, respectively. The subscript 'pt' denotes that this excess field originates from the periodic images of a point charge. Eq. (15) can be readily re-expressed in the Fourier space as follows:

$$E^{\text{ex}}_{\text{pt},z}(z_l) = \frac{1}{2\epsilon L_x L_y} \sum_{i=1}^{\infty} \sum_{\mathbf{m}\in\mathbb{Z}^2} q_i e^{-2\pi(z_l - z_i)\sqrt{\frac{m_x^2}{L_x^2} + \frac{m_y^2}{L_y^2}}} - \frac{1}{4\pi\epsilon} \sum_{i=1}^{\infty} \frac{q_i}{(z_l - z_i)^2} \tag{16}$$

Note that the inclusion of the last term is to ensure that only the contributions of the periodic replicates of the image charges are included.

A similar procedure can be employed to account for the effect of other ions in the membrane on the traversing ion. More precisely, let N be the number of such ions and let q'_j and z'_j be the charge and the position of the jth such ion. Also, denote the magnitudes and positions of its image charges with $(q'_{j,i}, z'_{j,i})$. The excess electric field due to periodic replicates of q'_j, as well as those of its image charges, will be given by:

$$E^{\text{ex}}_{\text{pt},z}\left(z_l | q'_j\right) = \frac{1}{4\pi\epsilon} \sum_{\substack{\mathbf{m}\in\mathbb{Z}^2 \\ \mathbf{m}\neq(\mathbf{0})}} \left[\frac{q'_j(z_l - z'_j)}{\left[m_x^2 L_x^2 + m_y^2 L_y^2 + (z_l - z'_j)^2\right]^{\frac{3}{2}}} + \sum_{i=1}^{\infty} \frac{q'_{j,i}(z_l - z'_{j,i})}{\left[m_x^2 L_x^2 + m_y^2 L_y^2 + (z_l - z'_{j,i})^2\right]^{\frac{3}{2}}} \right] \tag{17}$$

Note that the only difference between (15) and (17) is the inclusion of the periodic images of q'_j, as it constitutes a charge distinct from q.

The presence of all point charges (whether the traversing ion or all other ions in the membrane) will induce bound charges at the surfaces of the conducting domains. Assuming the conductor lies in region 1, the cumulative bound charge induced at its surface can be expressed as:

$$q_b = -\frac{1}{\epsilon_2} \sum_{i=1}^{\infty} \left[q_i + \sum_{j=1}^{N} q'_{j,i} \right], \tag{18}$$

Note that Eq. (18) is a generalization of Eq. (7) by acknowledging that $\gamma_{12} \to 1$ if $\epsilon_1 \to \infty$. If the conducting domain possesses a net charge q_{net}, an excess charge not accounted for by q_b will uniformly distribute across the surface(s) of the conductor, with its magnitude given by:

$$q_e = q_{\text{net}} - q_b \tag{19}$$

In a typical membrane separation system, the conducting domain will possess two surfaces located at $z_{c,b}$ and $z_{c,m}$. Each surface can be effectively represented as a uniform charge slab with a surface charge density $\sigma = q_e/2L_xL_y$. The excess electric field resulting from a uniform charge slab with a charge density σ_p and located at z_p is given by:

$$E^{\text{ex}}_{s,z}(z|\sigma_p, z_p) = \frac{\sigma_p}{4\pi\epsilon}\left[2\pi - \int_{-\frac{L_x}{2}}^{\frac{L_x}{2}}\int_{-\frac{L_y}{2}}^{\frac{L_y}{2}} \frac{(z-z_p)\,dx\,dy}{[x^2+y^2+(z-z_p)^2]^{\frac{3}{2}}}\right] \quad (20)$$

In Equation (20), the subscript s denotes that this field is induced by a uniform charge slab, and the second integral accounts for the contribution of the portion of the slab that is located inside the simulation box. The overall free energy correction profile can then be estimated from,

$$\Delta\mathcal{F}_{\text{corr}}(z) = -q\int_{z_0}^{z}\left[E^{\text{ex}}_{\text{pt},z}(\overline{z}) + \sum_{j=1}^{N} E^{\text{ex}}_{\text{pt},z}\left(\overline{z}|q'_j\right) + E^{\text{ex}}_{s,z}\left(\overline{z}\left|\frac{q_e}{2L_xL_y}, z_{c,b}\right.\right) + E^{\text{ex}}_{s,z}\left(\overline{z}\left|\frac{q_e}{2L_xL_y}, z_{c,m}\right.\right)\right] d\overline{z} \quad (21)$$

It is necessary to underscore that the positions of image charges for the traversing ion (as well as all other ions present within the membrane) will depend on z_l. Thus, it is more convenient to evaluate Eq. (21) through numerical methods.

As will be discussed in Section IV, the ICDM model can be readily extended to consider more complicated scenarios, but in all such cases, the extension can be constructed by considering the combined effect of point charges and slabs of uniformly distributed charges.

III. METHODS

This section outlines the methodological details of molecular simulations and rate calculations that are conducted with the aim of assessing the performance of the ICDM model.

A. System Preparation and Molecular Dynamics Simulations

In this study, we focus on model graphitic membranes featuring sub-nanometer pores passivated with hydrogen atoms. The membrane separates a feed compartment comprised of an aqueous sodium chloride solution from a filtrate initially comprised of pure water. Two pristine graphene sheets are employed as pistons that apply a hydrostatic pressure gradient between the two compartments. We consider systems with varying membrane cross-sectional surface areas, all while keeping constant the salt concentration, pore chemistry and geometry, as well as the thickness of the feed and the filtrate along the z direction. For each system size, we prepare 100 independent configurations, employing the PACKMOL[38] tool to randomize the positions of water molecules and salt ions. Water molecules are described using the TIP3P force-field,[39] while the behavior of salt ions is modeled using the Joung-Cheatham potential.[40] Interactions between membrane atoms are described using the parameters developed by Beu[41] and Müller-Plathe.[42] Further details about system setup can be found in our earlier publications.[18,19]

In all systems considered here, ion transport occurs in the presence of pressure and chemical potential gradients. Pressure gradient is applied using nonequilibrium molecular dynamics[43] (NEMD) wherein a net force is applied on the pistons. All NEMD simulations are conducted in LAMMPS[44] wherein Newton's equations of motion are integrated using the velocity Verlet algorithm and temperature is controlled using the Nosé-Hoover thermostat[45,46] with a damping constant of 0.1 ps. Periodic boundary conditions are only applied along the x and y dimensions, and long-range electrostatic interactions are handled using the slab particle-particle particle-mesh (PPPM) method to avoid known artifacts due to interactions between the system and its periodic images along the z direction.[47]

The 100 configurations prepared for each system are initially equilibrated with the piston held in place for a duration of 0.1 ns using a time step of 0.5 fs. The pistons are then allowed to move as rigid bodies to generate a pressure gradient of 194 atm. The time step is then increased to 1 fs and trajectories are extended for an additional 2 nanoseconds to complete equilibration.

B. Calculation of Ion Transport Timescales

Due to the rare nature of ion translocation in the systems considered here, we estimate transport timescales using the jumpy forward-flux sampling[48] (JFFS) algorithm, which allows us to access arbitrarily long translocation timescales with remarkable computational efficiency. One distinct advantage of forward flux sampling is its compatibility with irreversible integrators, which makes it suitable for studying driven processes such as pressure-driven ion transport.[49] The translocation processes considered here can be generally denoted by $F_{p,q} \rightarrow F_{p\pm1,q\pm1}$ wherein $F_{p,q}$ refers to a collection of configurations in which p sodiums and q chlorides are present within the filtrate. In particular, we examine the $F_{0,0} \rightarrow F_{0,1}$ and $F_{0,1} \rightarrow F_{1,1}$ transitions corresponding to the initial passage of a chloride (which is the counter-ion in this case) and the subsequent passage of a sodium (the co-ion). In both cases, we use the curved directed distance of the respective leading ion as the JFFS order parameter with details given in Ref. 18. For the $F_{0,0} \rightarrow F_{0,1}$ transitions, we use the structures arising from the equilibration procedure described above as starting configura-

tions for basin exploration. For the $F_{0,1} \rightarrow F_{1,1}$ transition, starting configurations are randomly selected from the crossing events obtained at the last JFFS milestone of the $F_{0,0} \rightarrow F_{0,1}$ transition.

In the new ICDM model proposed here, we still treat the feed compartment as an ideal conductor (i.e., with $\epsilon \rightarrow \infty$). It is therefore important to identify a proper value for z_c, the location of the conducting surface at which net or induced charge will accumulate, and z_b, the position of the conductor-piston interface. This is done using the approach outlined in Ref 19, which involves computing the background charge density in the feed within the $F_{0,0}$ basin, and subtracting it from charge densities obtained at different values of the order parameter. We find that the induced charge occupies the first two layers of water at the membrane surface. As such, z_c is chosen as the average position of the first two layers weighted by the amount of induced charge within each liquid layer. For z_b, we use the average position of the first layer of the liquid next to the piston. We, however, wish to note that the ICDM model is not very sensitive to the location of z_c and z_b.

Since this work aims to incorporate dielectric effects into finite size corrections, it is necessary to compute dielectric constants in different regions of the system. To that end, we use the technique described by Neumann[50] which utilizes fluctuations in the total dipole moment of the region ($\mathbf{M}$). The dielectric constant is then given as:

$$\epsilon = 1 + \frac{\langle |\mathbf{M}|^2 \rangle - |\langle \mathbf{M} \rangle|^2}{3\epsilon_0 k_b T \langle V \rangle} \tag{22}$$

where ϵ_0 is the vacuum permittivity, k_b is the Boltzmann constant, T is the temperature, and $\langle V \rangle$ is the volume of the region under consideration. Care must be taken in applying this approach to regions that can be partially occupied by a molecule. The dipole moment of an electrically neutral molecules is invariant with respect to the choice of coordinate system. As it moves further away from the reference point, the increased contribution of the positively-charged sub-components will be exactly compensated by an increased contribution of the negatively-charged sub-components in the opposite direction. However, if the molecule straddles the boundary of a region, this can lead to an unphysical spike in the dipole moment due to the unbalanced charge which may be far from the reference point. In order to avoid this, if the oxygen atom of a water molecule falls within the region of interest, the entire molecule is included in the calculation of the dipole moment for that region. Such a molecule is then excluded from the region that does not contain its oxygen.

IV. RESULTS

A. Comparison with the Ideal Conductor Model

We first compare the performance of the ICDM model with that of the ideal conductor model proposed in our earlier work.[19] Consistent with Ref. 19, we consider the $F_{0,0} \rightarrow F_{0,1}$ transition, i.e., the translocation of the first chloride through a hydrogen-passivated three-layer graphitic membrane. As depicted in Figure 3A, the uncorrected free energy profiles exhibit a pronounced sensitivity to system size. Not only do we observe a variation in the magnitude of the translocation barrier by as much as $13k_BT$, but the precise location of the barrier also shifts with changes in system size. Remarkably, the application of the original ideal conductor model yields a reasonable level of agreement among the corrected free energy profiles, particularly within the first half of the pore, as shown in Figure 3B. This is further underscored by the relatively consistent estimates of translocation barriers, varying by less than one k_BT, as depicted in Figure 3D and given in Table I. Nonetheless, the corrected profiles diverge to a small– but statistically significant– extent within the second half of the pore.

In order to assess the importance of the dielectric effects incorporated into the ICDM model and whether they can rectify the discrepancies in corrected free energy profiles, we partition the non-feed region of our simulation box into two distinct dielectric domains, representing the membrane and the filtrate. The dielectric constants for these two regions are computed using Eq. (22) and given in Table II. (Other model parameters are given in Table III.) Due to the large error bars in the estimated dielectric constants within the filtrate, we use $\epsilon_3 = 71.38$, i.e., the mean dielectric constant (across all system sizes) for all the corrections, as we have no reason to believe that the dielectric constant of the filtrate would change considerably across systems of different sizes. We estimate the correction profile given by Eq. (21), and since there are no other ions inside the pore during the translocation process, the second term within the integrand will vanish. As depicted in Figure 3C, the application of the ICDM model yields substantial enhancements in agreement and consistency across the corrected profiles. Most notably, it effectively resolves the divergence observed among the corrected profiles within the latter half of the pore, i.e., in close proximity to the pore exit.

The translocation barriers predicted by the ICDM model tend to be marginally smaller than those estimated from the ideal conductor model, suggesting that the latter modestly underestimates the magnitude of the free energy correction. They, however, exhibit a remarkable degree of consistency, with variations of only $\lesssim 0.5k_BT$. This stands in stark contrast to the ideal conductor model, which exhibits variability on the order of $\sim k_BT$. A more rigorous measure of variability among barriers estimated from different system sizes is the *coefficient of variation (CoV)*, which is the ratio of

TABLE I: Estimates of the ideal conductor model and the ICDM model for the translocation barrier and the passage time in the thermodynamic limit. Note that using the ICDM model improves the consistency between the estimated barriers and passage times across system sizes.

	Finite		Ideal conductor		ICDM	
$S\,[\mathrm{nm}^2]$	$\tau_{c,f}$ [ns]	$\beta\Delta\mathcal{F}_{c,f}$	$\beta\Delta\mathcal{F}_{c,\infty}$	$\tau_{c,\infty}$ [ns]	$\beta\Delta\mathcal{F}_{c,\infty}$	$\tau_{c,\infty}$ [ns]
12.53	$(8.29 \pm 0.53) \times 10^7$	19.40 ± 0.10	6.11 ± 0.12	140 ± 48	5.76 ± 0.10	99 ± 48
26.33	$(1.36 \pm 0.17) \times 10^4$	10.79 ± 0.06	7.05 ± 0.14	322 ± 117	5.99 ± 0.04	112 ± 44
32.60	$(3.38 \pm 0.17) \times 10^3$	9.41 ± 0.04	7.20 ± 0.14	372 ± 79	6.23 ± 0.11	141 ± 54
50.15	$(4.69 \pm 0.58) \times 10^2$	7.58 ± 0.08	6.86 ± 0.10	228 ± 68	5.90 ± 0.03	96 ± 33
100.28	$(1.12 \pm 0.16) \times 10^2$	6.63 ± 0.22	6.37 ± 0.22	86 ± 64	5.80 ± 0.24	49 ± 45

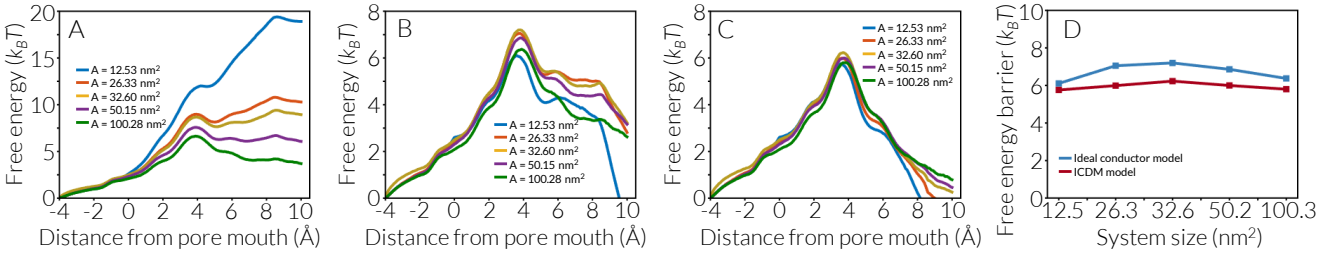

FIG. 3: (A) Original (uncorrected) free energy profiles for the $F_{0,0} \to F_{0,1}$ transition in the three-layer graphitic membrane considered in Ref. 19. (B-C) Corrected free energy profiles obtained from (B) the original ideal conductor model, and (C) the ICDM model using the dielectric constants given in Table II and parameters given in Table III. (D) The corrected translocation barriers predicted using the two models.

TABLE II: Dielectric constants for the membrane (ϵ_2) and filtrate (ϵ_3) regions computed using Eq. (22)

$S\,[\mathrm{nm}^2]$	ϵ_2	ϵ_3
12.53	1.339 ± 0.008	70.81 ± 1.31
26.33	1.183 ± 0.001	70.48 ± 1.89
32.6	1.144 ± 0.001	70.08 ± 3.54
50.15	1.095 ± 0.001	70.19 ± 2.49
100.28	1.050 ± 0.001	76.38 ± 5.68

the standard deviation of different observations, divided by their mean. The CoV of translocation barriers is 0.068 and 0.028 for the ideal conductor and the ICDM models, respectively.

All these findings underscore the heightened accuracy of the ICDM model relative to the original ideal conductor model. However, it is noteworthy that this superior accuracy is particularly consequential within segments of the free energy profile situated in close proximity to the filtrate. Conversely, for scenarios in which the transition state maintains a considerable distance from the membrane-filtrate interface, both models exhibit comparable performance. This is indeed the case for the $F_{0,0} \to F_{0,1}$ transition, where the transition state is positioned at approximately $z^* \approx 0.38\,\mathrm{nm}$. Notably, this location is situated ≈ 0.5 nm away from the membrane-filtrate interface, reaffirming the two models' comparable performance for the $F_{0,0} \to F_{0,1}$ transition.

B. Sensitivity to Implementation Details

In this section, we assess the sensitivity of ICDM model predictions to implementation details. The first question that we address is the rate of convergence, as applying the ICDM model requires evaluating two nested infinite series: the summation over all image charges and the consideration of periodic replicates of each image charge. In practice, however, this is achieved by truncating the infinite sums, necessitating the determination of the appropriate number of terms to ensure satisfactory convergence. It is worth noting that the number of image charges affects both Eq.(15) and Eq.(20), while the number of periodic replicates only impacts Eq. (15).

To assess the convergence characteristics of the ICDM correction concerning the number of image charges and periodic replicates, we compute the following finite sums for systems of varying sizes:

$$E^{\mathrm{ex}}_{\mathrm{pt},z}(z_l; n_{\mathrm{im}}, n_{\mathrm{prd}}) = \sum_{i=1}^{n_{\mathrm{im}}} \sum_{\substack{m_x, m_y = -n_{\mathrm{prd}} \\ \mathbf{m} \neq (\mathbf{0})}}^{n_{\mathrm{prd}}} \frac{q_i (z_l - z_i)}{4\pi\epsilon \left[m_x^2 L_x^2 + m_y^2 L_y^2 + (z_l - z_i)^2 \right]^{\frac{3}{2}}} \tag{23}$$

$$q_b(n_{\mathrm{im}}) = -\frac{1}{\epsilon_2} \sum_{i=1}^{n_{\mathrm{im}}} q'_i \tag{24}$$

We then investigate the impact of varying n_{im} and n_{prd} on the predicted corrected profiles and estimated translo-

TABLE III: Parameters utilized in the numerical implementation of the ICDM model. Uncertainties are negligible for parameters without error bars. All symbols are defined in the main text. Note that z_M, n_m and n_f are only relevant to the correction discussed in Section IV C.

S [nm^2]	z_0 [nm]	$z_{c,m}$ [nm]	$z_{c,b}$ [nm]	z_m [nm]	z_M [nm]	n_m	n_f
12.53	0	-0.504 ± 0.007	-4.225	0.87	3.60	2	6
26.33	0	-0.470 ± 0.027	-4.225	0.87	3.55	2	6
32.6	0	-0.483 ± 0.022	-4.225	0.87	3.55	2	6
50.15	0	-0.461 ± 0.023	-4.075	0.87	3.43	2	6
100.28	0	-0.452 ± 0.021	-4.325	0.87.	3.48	2	6

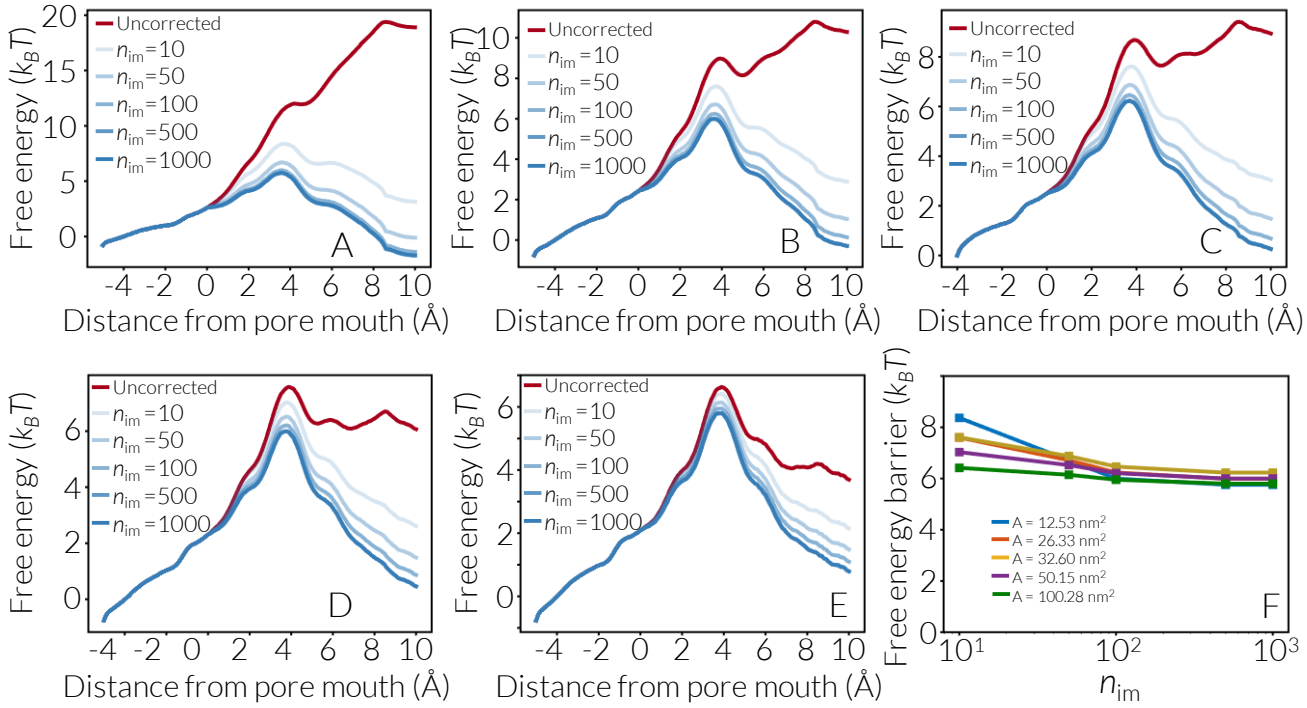

FIG. 4: The sensitivity of the ICDM correction to the number of image charges. Panels (A-E) illustrate the corrected profiles for systems with cross-sectional surface areas of (A) 12.53 nm^2, (B) 26.33 nm^2, (C) 32.60 nm^2, (D) 50.15 nm^2, and (E) 100.28 nm^2, when different numbers of image charges are utilized. (F) The calculated translocation barriers for various systems as a function of n_{im}, indicating satisfactory consistency when more than 100 image charges are included. These calculations employ $n_{\text{prd}} = 200$ periodic replicates, equivalent to 400 replicates in each direction.

cation barriers for each system, as illustrated in Figures 4 and 5. When it comes to image charges, we observe that satisfactory convergence is achieved with approximately $n_{\text{im}} \approx 100$ image charges. Including more image charges does not significantly alter the corrected free energy profiles (Figures 4A-E) or the estimated translocation barrier in the thermodynamic limit (Figure 4F). While this threshold might initially seem high, it is important to note that the need to include periodic replicates of image charges in the finite size correction can amplify otherwise minor truncation errors.

In contrast to the number of image charges, the number of periodic replicates required for satisfactory convergence varies with system size, as depicted in Figure 5, and is larger for small systems. This observation is consistent with our expectation, as the contribution of a particular periodic replicate to free energy correction is expected to diminish as the size of the simulation box increases. Across the range of system sizes investigated here, we find that satisfactory convergence is attained with approximately $n_{\text{prd}} \approx 50$, equivalent to 100 replicates in each direction. However, it is worth noting that smaller systems may require more terms for convergence due to the stronger impact of periodic replicates in such cases.

As discussed in Section II B, Eq. (15) can be alternatively expressed as an infinite sum in the Fourier space, given by Eq. (16). One might intuitively expect Eq.(16) to converge faster than Eq.(15) considering the fact it is comprised of exponentials instead of rational functions. However, our numerical tests reveal an interesting pattern. Eq.(16) indeed converges faster than Eq.(15) only for very small system sizes and at z_l's sufficiently distant

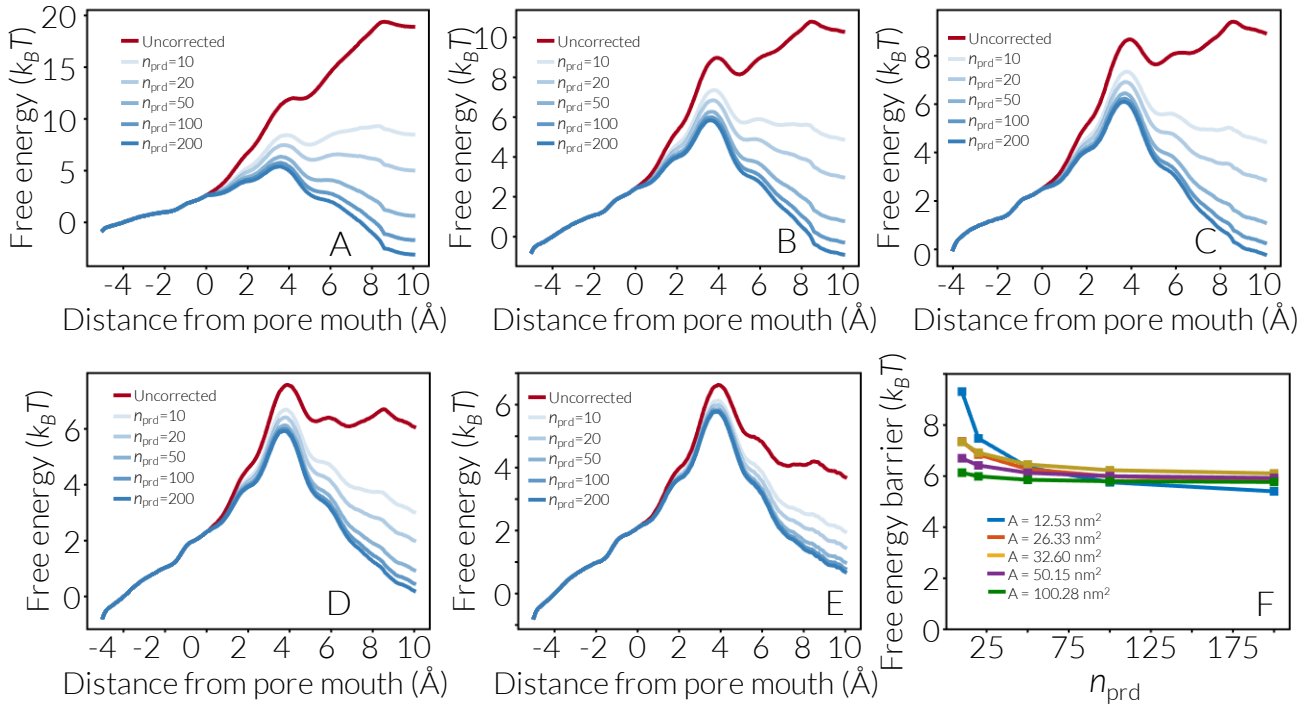

FIG. 5: The sensitivity of the ICDM correction to the number of periodic replicates. Panels (A-E) demonstrate corrected profiles for systems with cross-sectional surface areas of (A) 12.53 nm^2, (B) 26.33 nm^2, (C) 32.60 nm^2, (D) 50.15 nm^2 and (E) 100.28 nm^2 with different number of periodic replicates. (F) The calculated translocation barriers for various systems as a function of n_{prd}, indicating satisfactory consistency for $n_{\mathrm{prd}} \geq 50$. These calculations employ $n_{\mathrm{im}} = 1000$ image charges.

from dielectric-conductor and dielectric-dielectric interfaces. In particular, Eq. (16) becomes notoriously difficult to converge at close proximity of an interface, where $|z_l - z_i|$ becomes extremely small. Consequently, while more complex hybrid methods, akin to those employed in Ewald summation, can be devised, it is more reliable to calculate the correction in real space rather than Fourier space.

Another crucial parameter influencing the predictions of the ICDM model is z_0 in Eq. (21), which represents the initiation point for the application of the correction. Empirically, we select z_0 as the point at which uncorrected free energy profiles for various system sizes begin to diverge. As discussed in our earlier work,[19] this coincides with the approximate point at which the leading ion (along with its first hydration shell) fully departs from the feed region.

As depicted in Figure 6, corrected profiles exhibit the highest degree of consistency across different system sizes when $z_0 \approx 0$, the value that we had identified in Ref. 19 based on our physical intuition. However, it is noteworthy that the translocation barrier's magnitude and the coefficient of variation (CoV) among barriers obtained from different system sizes do not exhibit extreme sensitivity to the choice of z_0. For instance, employing $z_0 = 0.05\,\mathrm{nm}$ yields nearly identical barrier values (Figure 6E) and a comparable level of overall coefficient of variation (Figure 6F).

C. Application of the ICDM Model to Secondary Ion Transport Processes

Thus far, our main focus has been to utilize the ICDM model to probe the transport of the leading ion from a conducting compartment to a dielectric compartment with no ions. It must, however, be emphasized that the ICDM model can be readily extended to consider secondary ion transport scenarios, i.e., situations in which ions are already present on both sides of the membrane during the translocation process. As discussed earlier, extending the theory is straightforward when both reservoirs are concentrated enough to be considered ideal conductors. In such cases, the three-region description we have discussed here corresponds to a dielectric region positioned between two conductors, where $\epsilon_1 = \epsilon_3 \sim \infty$, with the electrostatic potential within the intermediate dielectric given by Eq. (13). It is, however, far more complex to extend the ICDM model to situations in which the filtrate contains too few ions to be considered an ideal conductor.

A good test case for the latter scenario is the $F_{0,1} \rightarrow F_{1,1}$ transition in the three-layer graphitic membrane considered in Ref. 19. The sub-nm pores considered

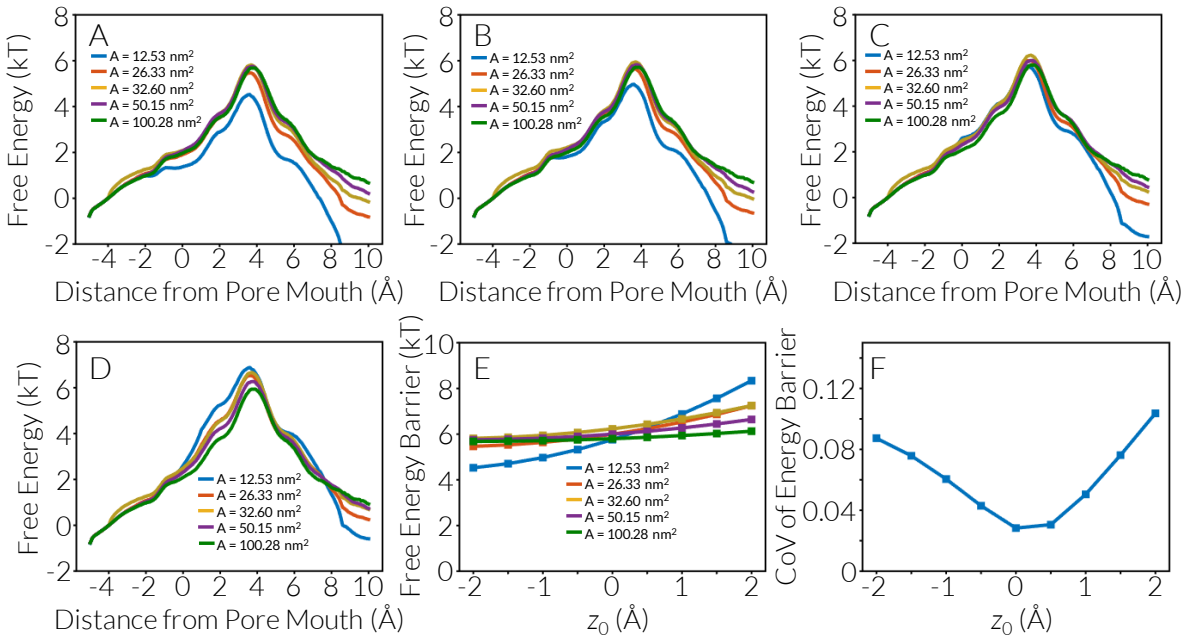

FIG. 6: Dependence of the corrected free energy profiles on z_0. (A-D) Corrected free energy profiles across different system sizes using (A) $z_0 = -0.2\,\text{nm}$, (B) $z_0 = -0.1\,\text{nm}$, (C) $z_0 = 0.0\,\text{nm}$ and (D) $z_0 = 0.1\,\text{nm}$. (E) Estimated translocation barriers in the thermodynamic limit as a function of z_0. (F) Coefficient of variation (CoV) of the estimated barrier across different system sizes vs. z_0.

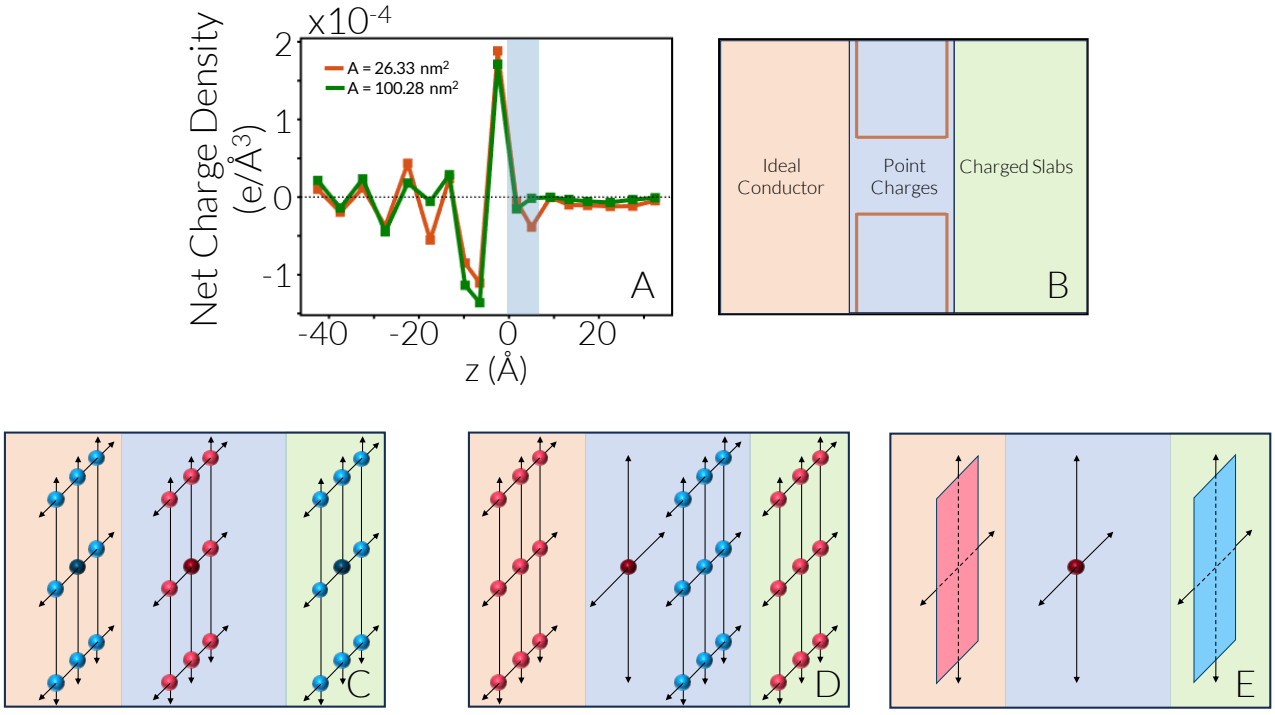

FIG. 7: (A) Net charge density as a function of distance from the pore mouth in the $F_{0,1}$ basin. (B) Schematic representation of the separation system, comprised of the conducting feed, the membrane (which can include extra point charges) and the dielectric filtrate (that contains the leading chloride). (C-D) Image charges induced by (C) the leading sodium and (D) the leading chloride that reenters the pore within the conducting feed and the dielectric filtrate. (E) Slabs of uniformly distributed chlorides inside the filtrate and the image charges they induce within the feed.

therein are passivated by hydrogen atoms with partial positive charges, and, as such, prefer chloride ions over sodiums. After the passage of the first chloride, however, a transmembrane electrostatic potential is established that favors sodium transport. Similar to the $F_{0,0} \rightarrow F_{0,1}$ transition, the periodic replicates of the image charges of the traversing sodium within the conducting feed and dielectric filtrate will give rise to finite size artifacts (Figure 7C), and these effects can be readily captured using the ICDM model presented above. There are, however, additional finite size artifacts that arise from interactions between the leading sodium and the periodic replicates of the leading chloride that is already in the filtrate. More precisely, such replicates will exert unphysical forces on the leading sodium, which will pull it into the filtrate, thus artificially lowering the free energy barrier. Furthermore, the leading chloride will also generate induced charge within neighboring regions, and the periodic replicates of those will also generate unphysical forces on the leading sodium.

In order to characterize the influence of the leading chloride ion on the passage of the leading sodium, it is essential to examine the spatial distribution of the former within both the membrane and the filtrate. Figure 7A illustrates the charge density variation with respect to the z coordinate before the leading sodium enters the pore. Note that any deviations from zero within the membrane and filtrate regions will arise due to the presence of the chloride ion. The leading chloride is primarily located within the filtrate, but occasional instances occur where it is drawn back into the pore due to favorable electrostatic interactions.

To account for induced charges within the conducting and dielectric regions, these two scenarios must be treated differently. When the leading chloride resides within the membrane (Figure 7D), it can be treated as a point charge positioned along the central axis of the pore. The magnitude of this point charge is equivalent to the average total charge within the corresponding spatial bin. This treatment yields a series of point charges $\mathcal{C}_m = \{(q_{m,j}, z_{m,j})\}_{j=1}^{n_m}$, where n_m corresponds to the number of spatial bins within the pore. The image charges associated with each point charge in $\mathcal{C}_m$ are then determined using the procedure outlined in Section II A, and their contributions to the free energy correction are enumerated using Eq. (17).

When it comes to the chloride within the filtrate, we can evaluate a charge density function $\rho_f(x,y,z)$ and identify a sequence of image functions $[\rho_{f,i}(x,y,z), z_i(z)]_{i=1}^{+\infty}$. The excess electric field can then be estimated as follows:

$$E_{f,z}^{\text{ex}}(z_l) = \int_{-\frac{L_x}{2}}^{\frac{L_x}{2}} \int_{-\frac{L_y}{2}}^{\frac{L_y}{2}} \int_{z_m}^{z_M} dx\, dy\, dz \left[\sum_{i=1}^{+\infty} \sum_{\substack{\mathbf{m}\in\mathbb{Z}^2 \\ \mathbf{m}\neq\mathbf{0}}} \frac{\rho_{f,i}(x,y,z)\,[z_l - z_i(z)]}{4\pi\epsilon_0\epsilon_2 \left[(x+m_x L_x)^2 + (y+m_y L_y)^2 + [z_l - z_i(z)]^2 \right]^{\frac{3}{2}}} \right] \tag{25}$$

Here, z_m and z_M represent the boundaries of the membrane region. Notably, the sodium inside the pore does not directly experience the impact of $\rho_f(x,y,z)$, as the original charge profile is screened by the induced charges at dielectric interfaces. Consequently, the correction profile is given by:

$$\begin{aligned} \mathcal{F}_{\text{corr}}(z) \;=\; -q_s \int_{z_0}^{z} \Bigg[& E_{\text{pt},z}^{\text{ex}}(\overline{z}) + \sum_{j=1}^{n_m} E_{\text{pt},z}^{\text{ex}}(\overline{z}|j) \\ & + E_{f,z}^{\text{ex}}(\overline{z}) + E_{e,z}^{\text{ex}}\left(\overline{z}\,\middle|\,\frac{q_e}{2L_xL_y}, z_{c,p}\right) \\ & + E_{e,z}^{\text{ex}}\left(\overline{z}\,\middle|\,\frac{q_e}{2L_xL_y}, z_{c,m}\right) \Bigg] d\overline{z} \end{aligned} \tag{26}$$

Here, q_s corresponds to the charge of the leading sodium. While this framework is theoretically rigorous, its practical implementation is challenging due to difficulties in accurately estimating $\rho_f(x,y,z)$ with necessary resolution. Thus, we adopt a simplified approach in which the filtrate is divided into slabs, and chloride concentration within each slab is assumed constant. This assumption is based on the observation that, at any given z, chloride concentration depends weakly on x and y. This simplified model yields n_f charge slabs with positions and surface charge densities denoted as $z_{f,i}$ and $\sigma_{f,i}$, respectively (Figure 7E). The corresponding simplified correction will then be given by:

$$\begin{aligned} \mathcal{F}_{\text{corr}}^{\text{slab}}(z) \;=\; -q_s \int_{z_0}^{z} \Bigg[& E_{\text{pt},z}^{\text{ex}}(\overline{z}) + \sum_{j=1}^{n_m} E_{\text{pt},z}^{\text{ex}}(\overline{z}|j) \\ & + \sum_{j=1}^{n_f} E_{e,z}^{\text{ex}}(\overline{z}|\sigma_{f,i}, z_{f,i}) \\ & + E_{e,z}^{\text{ex}}\left(\overline{z}\,\middle|\,\frac{q_e}{2L_xL_y}, z_{c,p}\right) \\ & + E_{e,z}^{\text{ex}}\left(\overline{z}\,\middle|\,\frac{q_e}{2L_xL_y}, z_{c,m}\right) \Bigg] d\overline{z} \end{aligned} \tag{27}$$

Here, the superscript 'slab' refers to the fact that the correction given by Eq. (27) is obtained by making the slab approximation. By analyzing the configurations collected at each FFS milestone, we can estimate $q_{m,j}$ and $\sigma_{f,j}$ for the corresponding order parameter values. For intermediate z values, the charge densities from the nearest FFS milestone can be employed.

Figure 8A illustrates uncorrected free energy profiles for sodium transport after a chloride has already traversed the pore, with the uncorrected passage times and

TABLE IV: The translocation timescales and free energy barriers for the $F_{0,1} \rightarrow F_{1,1}$ transition obtained from JFFS, alongside the corrected values computed upon applying the ICDM model.

S [nm^2]	$\tau_{s,f}$ [s]	$\beta\Delta\mathcal{F}_{s,f}$	$\beta\Delta\mathcal{F}_{s,\infty}$	$\tau_{s,\infty}$ [s]
26.33	6.70 ± 0.35	19.96 ± 0.10	22.91 ± 0.25	172 ± 85
100.28	576.14 ± 98.4	23.07 ± 0.28	23.70 ± 0.14	1077 ± 733

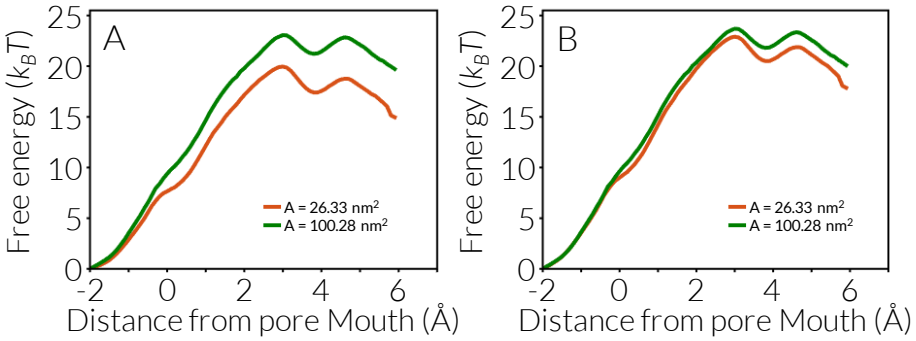

FIG. 8: (A) Uncorrected and (B) corrected free energy profiles for the $F_{0,1} \rightarrow F_{1,1}$ transition. The correction has been applied using Eq. (27).

barriers given in Table IV. Similar to chloride transport, substantial finite size effects are evident in sodium transport as well. However, these finite size effects manifest in the opposite direction, causing smaller systems to exhibit artificially lower translocation barriers. Upon applying, the simplified correction scheme described by Eq. (27), the corrected free energy profiles, showcased in Figure 8B exhibit remarkable agreement across system sizes. These findings not only demonstrate the efficacy of the ICDM model but also indicate that the largest system studied in this context is sufficiently large to exhibit acceptable convergence to the thermodynamic limit.

We wish to note that the reversal in the direction of finite size effects in secondary ion translocation processes implies that the strategy of simulating a sufficiently large system that is devoid of noticeable finite size effects might be prohibitively expensive computationally. For instance, in the case of the system with 100.28 nm^2 cross-sectional surface area, the cumulative length of trial MD trajectories conducted as part of JFFS reaches a whopping 62 μs. In contrast, the smaller system with 26.33 nm^2 surface area requires a comparatively shorter 8.7 μs of trial MD trajectories to finish the same calculation. Assuming a linear scaling between system size and computational cost, the rate calculation in the larger system will be 27 times more expensive computationally. In light of these computational challenges, having an accurate and rigorous procedure for correcting finite size artifacts becomes essential. Such corrections not only ensure accuracy but also enable more efficient translocation rate calculations, allowing researchers to tackle complex systems with increased computational efficiency.

D. The Advantage of the Three-region ICDM Model

In all calculations considered here, we employ the version of the ICDM model with three regions (one conductor, and two dielectric domains). In principle, the accuracy of the ICDM model can be improved by partitioning the simulation box into more than three regions. There are, however, two major impediments to the success of such a strategy. The first problem is the scaling of the number of image charges with the number of regions. For a system with three regions, the scaling is linear as four image charges are added to the system per iteration. When $m > 3$, however, such a scaling is exponential (Figure 9A). Since the convergence of the method of images depends on the number of iterations, such exponential scaling will increase the memory and computational costs of convergence. This will not, however, be an issue when all domains possess modest dielectric constants. As can be seen in Figure 9B, while more image charges are necessary for convergence in 4- and 5-region domains, convergence is still achieved after around 35 iterations. The situation is, however, different when one of the regions is an ideal conductor (Figures 9C-E). Among all boundary conditions, the convergence of the electrostatic potential at a conductor's interface is extremely difficult and is never achieved when $m \geq 4$ (Figures 9D-E).

This slow convergence can be explained by the fact that the image charges generated across a conductor-dielectric interface will bear the same magnitude of the original charge albeit with the opposite sign, which will inadvertently slow down the rate of convergence. The problem

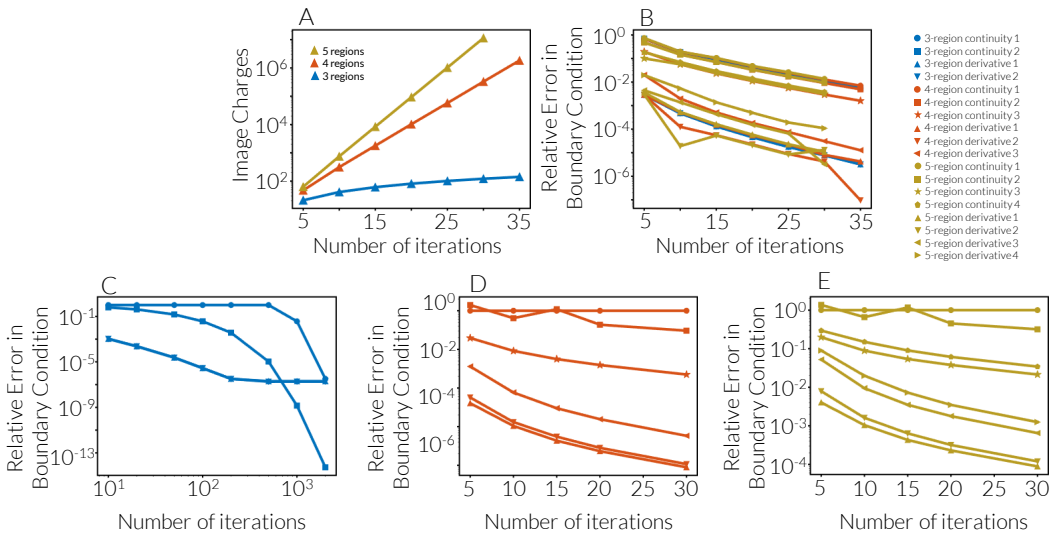

FIG. 9: (A) The total number of image charges as a function of the number of iterations in systems with $m = 3, 4$ and 5 dielectric domains. (B) The convergence of Algorithm 1 when all regions have modest dielectric constants, namely $(\epsilon_1, \epsilon_2, \epsilon_3) = (20, 1, 20)$, $(\epsilon_1, \epsilon_2, \epsilon_3, \epsilon_4) = (20, 1, 10, 20)$ and $(\epsilon_1, \epsilon_2, \epsilon_3, \epsilon_4, \epsilon_5) = (20, 1, 10, 15, 20)$ for $m = 3, 4$ and 5, respectively. As can be noted, a reasonably small relative error is obtained for all boundary conditions after 35 iterations. (C-E) The convergence of the algorithm when $\epsilon_1 = 2 \times 10^9$. The other dielectric constants are given by: (C) $(\epsilon_2, \epsilon_3) = (1.16, 70.5)$ for $m = 3$, (D) $(\epsilon_2, \epsilon_3, \epsilon_4) = (1.16, 82, 70.5)$ for $m = 4$, and (E) $(\epsilon_2, \epsilon_3, \epsilon_4, \epsilon_5) = (1.16, 88.3, 82, 70.5)$ for $m = 4$. Except for (C), the convergence at the conductor surface is not achieved even after including millions of image charges.

might be remedied by solving the Poisson's equation numerically (for different positions of the leading ion) and use that solution to estimate the correction. One might also be able to develop more efficient algorithms based on the method of images in which image charges are selectively added to regions for which the boundary conditions are the slowest to converge. In order to avoid such complexities, however, it is easier to use a three-region description unless it is absolutely necessary to include more regions otherwise.

The second challenge is the difficulty in computing profiles of dielectric constant in confined systems.[51] More precisely, Eq. (22) can only provide an accurate estimate of the local dielectric constant when the corresponding domain is large enough to be devoid of considerable spatial correlations in dipole fluctuations. Developing more efficient algorithms for computing profiles of dielectric tensors in confined geometries is key to successful execution of such a correction strategy.

V. CONCLUSIONS

In this work, we focus on the issue of polarization-induced finite size artifacts in molecular simulations of ion transport. To mitigate these effects, we introduce the ideal conductor dielectric model (ICDM), an extension of our earlier ideal conductor model that takes into account dielectric effects arising from charge induction due to dielectric heterogeneities within the membrane system. Our numerical tests demonstrate the significant improvements achieved by the ICDM model in enhancing the agreement among corrected free energy profiles computed for different system sizes, particularly in regions adjacent to the dielectric filtrate. A comparative analysis reveals that our original model slightly overestimates the corrected translocation barriers. Notably, the ICDM model showcases its versatility by accommodating secondary ion transport events, including the passage of co-ions through charge-selective nanopores, a feature absent in our initial model.

The ability to precisely address finite size effects in secondary ion translocation events is imperative for a comprehensive understanding of membrane selectivity in separation applications. Indeed, the transport of ionic solute across membranes proceeds through a series of sequential translocation events, commencing with the leading ion (accounted for by our original ideal conductor model), and followed by successive ion translocations from a conductor to a dielectric medium. In particular, it is typically the translocation of co-ions that consistently represents the rate-limiting step in solute transport. Accurate characterization of co-ion transport is therefore pivotal for predicting crucial properties such as salt rejection rates in desalination membranes.

There are multiple perils to not properly correcting the strong finite size effects discussed here and in our earlier work[19]. In addition to resulting in unrealistic predictions about the performance of ion separation membranes, they could also lead to qualitatively inaccurate

conclusions about how different membrane features impact selectivity. This is because the magnitude of finite size effects does not depend on lateral box dimensions only, and are impacted by the thickness and the dielectric properties of the membrane, the intrusion of additional ions, the ionic distribution in the feed and the filtrate, and the location of the transition state within the membrane. Consequently, membranes with identical cross sectional surface areas but with different pore chemistries and geometries will likely differ in the extent to which they will be impacted by finite size artifacts. This warrants caution in interpreting the findings of molecular simulations of nanoscale transport, particularly those in which different membranes are rank-ordered in terms of their selectivity. It also underscores the importance of finite size corrections in molecular simulations aimed at designing membranes with superior ion separation properties.

The success of the ICDM model in correcting for finite size artifacts implies that classical electrostatic theories based on continuum approximations perform remarkably well in systems of charged particles. This is in contrast to other continuum theories (such as fluid mechanics) that tend to be violated at the nanoscale. As to whether the success of electrostatic theories point to granular agreement at the microscopic level (i.e., the density and distribution of induced charges at dielectric interfaces) or is a consequence of fortuitous cancelation of errors is an interesting fundamental question that can be the subject of future studies.

In principle, it must be possible to avoid finite size artifacts by simulating systems that are sufficiently large. Considering the long-range nature of electrostatic interactions, however, the finite size effects identified here tend to vanish slowly with system size and are thus present (albeit to a smaller extent) even in very large systems. For instance, the translocation barrier in the 100.28 nm^2 system (comprised of over 22,000 water molecules) is $\approx 0.8 k_B T$ larger than the predicted barrier in the thermodynamic limit. Therefore, avoiding polarization-induced finite size effects by simulating larger systems can be computationally burdensome. This is particularly problematic in co-ion transport wherein the translocation timescale increases as the system size becomes larger. As discussed earlier, it is 27 times more computationally costly to compute the $F_{0,1} \rightarrow F_{1,1}$ timescale in the 100.28 nm^2 system than in the 26.33 nm^2 system. The main advantage of our ICDM model is that it allows one to infer reasonably accurate information about the behavior of the pore in the thermodynamic limit by conducting less expensive simulations of smaller systems.

Acknowledgements

A.H.-A. gratefully acknowledges the support of the National Science Foundation Grants CBET-1751971 (CAREER Award) and CBET-2024473. B.S. acknowledges the support of the Goodyear Tire & Rubber Fellowship. This work was supported as part of the Center for Enhanced Nanofluidic Transport (CENT), an Energy Frontier Research Center funded by the U.S. Department of Energy, Office of Science, Basic Energy Sciences under award no. DE-SC0019112. We thank P. G. Debenedetti, M. Elimelech, D. Laage, and B. Uralcan for useful discussions. These calculations were performed on the Yale Center for Research Computing. This work used the Extreme Science and Engineering Discovery Environment (XSEDE), which is supported by National Science Foundation grant no. ACI-1548562.[52]

Appendix A: The Convergence Properties of Eq. (13)

For simplicity, we analyze the convergence of Eq. (13) at $\mathbf{r} = z\mathbf{e}_z$, but the approach employed here can be readily extended to other positions. The electrostatic potential will thus be given by:

$$\varphi_2(z) \;=\; \frac{q}{4\pi\epsilon_0\epsilon_2}\left[\frac{1}{|z-h|} + \sum_{k=1}^{\infty} a_k(z)\right] \qquad \text{(A1)}$$

with $a_k(z)$ given by:

$$\begin{aligned} a_k(z) \;&=\; \frac{1}{|z-h+2kw|} + \frac{1}{|z-h-2kw|} \\ &\quad - \frac{1}{|z+h+2(k-1)w|} - \frac{1}{|z+h-2kw|} \\ &=\; \frac{1}{2kw}\left[\frac{1}{\left|1+\frac{z+h}{2kw}\right|} + \frac{1}{\left|1-\frac{z-h}{2kw}\right|}\right. \\ &\quad \left. - \frac{1}{\left|1+\frac{z+h-2w}{2kw}\right|} - \frac{1}{\left|1-\frac{z+h}{2kw}\right|}\right] \end{aligned}$$

For sufficiently large k, all the fractions inside absolute values will be small. One can therefore use Taylor expansion $|1+x|^{-1} \sim 1-x$ to conclude that:

$$a_k(z) \;\approx\; -\frac{h+w}{2k^2w^2} \qquad \text{(A2)}$$

which implies that the convergence rate of Eq. (13) is as fast as $\sum_{k=1}^{\infty} k^{-2}$.

[1] R. MacKinnon, FEBS Lett. **555**, 62 (2003), URL https://doi.org/10.1016/S0014-5793(03)01104-9.

[2] S. D. Tyerman, S. A. McGaughey, J. Qiu, A. J. Yool, and C. S. Byrt, Annu. Rev. Plant Biol. **72**, 703 (2021), URL https://doi.org/10.1146/annurev-arplant-081720-013608.

[3] R. Tan, A. Wang, R. Malpass-Evans, R. Williams, E. W. Zhao, T. Liu, C. Ye, X. Zhou, B. P. Darwich, Z. Fan, et al., Nat. Mater. **19**, 195 (2020), URL https://doi.org/10.1038/s41563-019-0593-z.

[4] P. Xiong, L. Zhang, Y. Chen, S. Peng, and G. Yu, Angew. Chem. Int. Edit. **60**, 24770 (2021), URL https://doi.org/10.1002/anie.202105619.

[5] K.-D. Kreuer, Chem. Mater. **26**, 361 (2014), URL https://doi.org/10.1021/cm402742u.

[6] A. Giwa, N. Akther, V. Dufour, and S. W. Hasan, RSC Adv. **6**, 8134 (2016), URL https://dx.doi.org/10.1039/C5RA17221G.

[7] M. Thomas, B. Corry, and T. A. Hilder, Small **10**, 1453 (2014), URL https://doi.org/10.1002/smll.201302968.

[8] M. T. H. van Vliet, E. R. Jones, M. Flörke, W. H. P. Franssen, N. Hanasaki, Y. Wada, and J. R. Yearsley, Env. Res. Lett. **16**, 024020 (2021), URL https://dx.doi.org/10.1088/1748-9326/abbfc3.

[9] P. Gerland, A. E. Raftery, H. Ševčíková, N. Li, D. Gu, T. Spoorenberg, L. Alkema, B. K. Fosdick, J. Chunn, N. Lalic, et al., Science **346**, 234 (2014), URL https://dx.doi.org/10.1126/science.1257469.

[10] C. He, Z. Liu, J. Wu, X. Pan, Z. Fang, J. Li, and B. A. Bryan, Nat. Comm. **12**, 4667 (2021), URL https://doi.org/10.1038/s41467-021-25026-3.

[11] L. Gudmundsson, S. I. Seneviratne, and X. Zhang, Nat. Clim. Change **7**, 813 (2017), URL https://doi.org/10.1038/nclimate3416.

[12] E. Jones, M. Qadir, M. T. van Vliet, V. Smakhtin, and S. mu Kang, Sci. Total Environ. **657**, 1343 (2019), URL https://doi.org/10.1016/j.scitotenv.2018.12.076.

[13] M. Elimelech and W. A. Phillip, Science **333**, 712 (2011), URL https://dx.doi.org/10.1126/science.1200488.

[14] A. Panagopoulos, K.-J. Haralambous, and M. Loizidou, Sci. Total Environ. **693**, 133545 (2019), URL https://doi.org/10.1016/j.scitotenv.2019.07.351.

[15] S. Jiang, Y. Li, and B. P. Ladewig, Sci. Total Environ. **595**, 567 (2017), URL https://doi.org/10.1016/j.scitotenv.2017.03.235.

[16] D. Cohen-Tanugi and J. C. Grossman, Nano Lett. **12**, 3602 (2012), URL https://doi.org/10.1021/nl3012853.

[17] D. Cohen-Tanugi and J. C. Grossman, Desalination **366**, 59 (2015), URL https://doi.org/10.1016/j.desal.2014.12.046.

[18] H. Malmir, R. Epsztein, M. Elimelech, and A. Haji-Akbari, Matter **2**, 735 (2020), ISSN 2590-2385, URL https://doi.org/10.1016/j.matt.2019.12.022.

[19] B. A. Shoemaker, T. S. Domingues, and A. Haji-Akbari, J. Chem. Theory Comput. **18**, 7142 (2022), URL https://doi.org/10.1021/acs.jctc.2c00375.

[20] C. Sun and B. Bai, Sci. Bull. **62**, 554 (2017), URL https://doi.org/10.1016/j.scib.2017.03.004.

[21] A. Nalaparaju and J. Jiang, J. Phys. Chem. C **116**, 6925 (2012), URL https://doi.org/10.1021/jp210082f.

[22] E. Harder, D. E. Walters, Y. D. Bodnar, R. S. Faibish, and B. Roux, J. Phys. Chem. B **113**, 10177 (2009), URL https://doi.org/10.1021/jp902715f.

[23] M. Shen, S. Keten, and R. M. Lueptow, J. Memb. Sci. **506**, 95 (2016), URL https://doi.org/10.1016/j.memsci.2016.01.051.

[24] F. Khalili-Araghi, J. Gumbart, P.-C. Wen, M. Sotomayor, E. Tajkhorshid, and K. Schulten, Curr. Opin. Struc. Biol. **19**, 128 (2009), URL https://doi.org/10.1016/j.sbi.2009.02.011.

[25] F. Zhu, E. Tajkhorshid, and K. Schulten, Biophys. J. **86**, 50 (2004), URL https://dx.doi.org/10.1016/S0006-3495(04)74082-5.

[26] J. S. Hub and B. L. de Groot, Biophys. J. **91**, 842 (2006), URL https://doi.org/10.1529/biophysj.106.081406.

[27] J. S. Hub and B. L. De Groot, Proc. Natl. Acad. Sci. USA **105**, 1198 (2008), URL https://doi.org/10.1073/pnas.0707662104.

[28] I. Kim and T. W. Allen, Proc. Natl. Acad. Sci. USA **108**, 17963 (2011), URL https://doi.org/10.1073/pnas.1110735108.

[29] E. B. Nordquist, Z. Jia, and J. Chen, Biophys. J. **122**, 1158 (2023), URL https://doi.org/10.1016/j.bpj.2023.02.005.

[30] S. H. Jamali, L. Wolff, T. M. Becker, A. Bardow, T. J. Vlugt, and O. A. Moultos, J. Chem. Theory Comput. **14**, 2667 (2018), URL https://doi.org/10.1021/acs.jctc.8b00170.

[31] A. T. Celebi, S. H. Jamali, A. Bardow, T. J. H. Vlugt, and O. A. Moultos, Mol. Simulat. **47**, 831 (2021), URL https://doi.org/10.1080/08927022.2020.1810685.

[32] J. J. Salacuse, A. R. Denton, and P. A. Egelstaff, Phys. Rev. E **53**, 2382 (1996), URL https://dx.doi.org/10.1103/PhysRevE.53.2382.

[33] J. Horbach, W. Kob, K. Binder, and C. A. Angell, Phys. Rev. E **54**, R5897 (1996), URL https://doi.org/10.1103/PhysRevE.54.R5897.

[34] G. Ahlers and R. V. Duncan, Phys. Rev. Lett. **61**, 846 (1988), URL https://doi.org/10.1103/PhysRevLett.61.846.

[35] K. Momeni, G. M. Odegard, and R. S. Yassar, Acta Materialia **60**, 5117 (2012), URL https://doi.org/10.1016/j.actamat.2012.06.041.

[36] S. Hussain and A. Haji-Akbari, J. Chem. Phys. **154**, 014108 (2021), URL https://doi.org/10.1063/5.0026355.

[37] S. Hussain and A. Haji-Akbari, J. Chem. Phys. **156**, 054503 (2022), URL https://doi.org/10.1063/5.0079702.

[38] L. Martínez, R. Andrade, E. G. Birgin, and J. M. Martínez, J. Comput. Chem. **30**, 2157 (2009).

[39] D. J. Price and C. L. Brooks III, J. Chem. Phys. **121**, 10096 (2004), URL https://doi.org/10.1063/1.1808117.

[40] I. S. Joung and T. E. Cheatham III, J. Phys. Chem. B **112**, 9020 (2008), URL https://doi.org/10.1021/jp8001614.

[41] T. A. Beu, J. Chem. Phys. **132**, 164513 (2010), URL https://doi.org/10.1063/1.3387972.

[42] F. Müller-Plathe, Macromolecules **29**, 4782 (1996), URL

https://doi.org/10.1021/ma9518767.
[43] T. D. Nguyen, J.-M. Y. Carrillo, A. V. Dobrynin, and W. M. Brown, J. Chem. Theory Comput. **9**, 73 (2013), URL https://doi.org/10.1021/ct300718x.
[44] S. Plimpton, J. Comput. Phys. **117**, 1 (1997), URL https://dx.doi.org/10.1002/nag.2347.
[45] S. Nosé, Mol. Phys. **52**, 255 (1984), URL http://dx.doi.org/10.1080/00268978400101201.
[46] W. G. Hoover, Phys. Rev. A **31**, 1695 (1985), URL http://dx.doi.org/10.1103/PhysRevA.31.1695.
[47] D. Bostick and M. L. Berkowitz, Biophys. J. **85**, 97 (2003), URL https://doi.org/10.1016/S0006-3495(03)74458-0.
[48] A. Haji-Akbari, J. Chem. Phys. **149**, 072303 (2018), URL https://doi.org/10.1063/1.5018303.
[49] S. Hussain and A. Haji-Akbari, J. Chem. Phys. **152**, 060901 (2020), URL https://doi.org/10.1063/1.5127780.
[50] M. Neumann, Mol. Phys. **50**, 841 (1983), URL https://doi.org/10.1080/00268978300102721.
[51] J.-F. Olivieri, J. T. Hynes, and D. Laage, J. Phys. Chem. Lett. **12**, 4319 (2021), URL https://doi.org/10.1021/acs.jpclett.1c00447.
[52] J. Towns, T. Cockerill, M. Dahan, I. Foster, K. Gaither, A. Grimshaw, V. Hazlewood, S. Lathrop, D. Lifka, G. D. Peterson, et al., Comput. Sci. Eng. **16**, 62 (2014), URL https://dx.doi.org/10.1109/MCSE.2014.80.